

Article

Semi-Embedding Zn-Co₃O₄ Derived from Hybrid ZIFs into Wood-Derived Carbon for High-Performance Supercapacitors

Wanning Xiong^{1,†}, Jie Ouyang^{1,†}, Xiaoman Wang¹, Ziheng Hua¹, Linlin Zhao¹, Mengyao Li¹, Yuxin Lu¹, Wei Yin¹, Gonggang Liu^{1,*}, Cui Zhou¹, Yongfeng Luo^{1,*}  and Binghui Xu² 

¹ Hunan Province Key Laboratory of Materials Surface & Interface Science and Technology, College of Science, Material Science and Engineering School, Central South University of Forestry and Technology, Changsha 410004, China

² Institute of Materials for Energy and Environment, School of Materials Science and Engineering, Qingdao University, Qingdao 266071, China

* Correspondence: liugonggang@csuft.edu.cn (G.L.); yfluo@csuft.edu.cn (Y.L.)

† These authors contributed equally to this work.

Abstract: Transition metal oxides (TMOs) can provide high theoretical capacitance due to the change of multiple valence states of transition metals. However, their intrinsic drawbacks, including poor electrical conductivity, lower energy density, and huge volume expansion, will result in the pulverization of electrode materials and restricted electrochemical kinetics, thus leading to poor rate capability and rapid capacity fading. Composite electrodes based on transition metal oxides and carbon-based materials are considered to be promising candidates for overcoming these limitations. Herein, we reported a preparation method of hybrid ZIFs derived Zn-doped Co₃O₄/carbon (Zn-Co₃O₄/C-230) particles semi-embedded in wood-derived carbon skeleton for integrated electrodes. A large specific surface area, excellent conductivity, and electrochemical stability provide a larger electrochemical activity and potential window for the electrode. Prepared Zn-Co₃O₄@CW-230 electrode (0.6 mm thick) displays ultrahigh area specific capacitances of 7.83 and 6.46 F cm⁻² at the current densities of 5 and 30 mA cm⁻², respectively. Moreover, a symmetric supercapacitor assembled by two identical Zn-Co₃O₄@CW-230 electrodes delivers a superior area-specific capacitance of 2.61 F cm⁻² at the current densities of 5 mA cm⁻² and great energy densities of 0.36 mWh cm⁻² (6.0 mWh cm⁻³) at 2.5 mW cm⁻², while maintaining 97.3% of initial capacitance over 10,000 cycles. It notably outperforms those of most carbon-based metal oxides, endowing the Zn-Co₃O₄@CW-230 with extensive prospects for practical application.

Keywords: semi-embedding; transition metal oxides; hybrid ZIFs; wood-derived carbon; supercapacitors



Citation: Xiong, W.; Ouyang, J.; Wang, X.; Hua, Z.; Zhao, L.; Li, M.; Lu, Y.; Yin, W.; Liu, G.; Zhou, C.; et al. Semi-Embedding Zn-Co₃O₄ Derived from Hybrid ZIFs into Wood-Derived Carbon for High-Performance Supercapacitors. *Molecules* **2022**, *27*, 8572. <https://doi.org/10.3390/molecules27238572>

Academic Editor: Tifeng Xia

Received: 4 November 2022

Accepted: 26 November 2022

Published: 5 December 2022

Publisher's Note: MDPI stays neutral with regard to jurisdictional claims in published maps and institutional affiliations.



Copyright: © 2022 by the authors. Licensee MDPI, Basel, Switzerland. This article is an open access article distributed under the terms and conditions of the Creative Commons Attribution (CC BY) license (<https://creativecommons.org/licenses/by/4.0/>).

1. Introduction

A supercapacitor (SC) is considered one of the potential candidates in the field of future generations of energy storage devices due to its high specific capacitance, excellent charge-discharge performance, and stable cycle performance [1–4]. The innovation of electrode materials is a key link to improving the performance of supercapacitors. In recent years, to further improve the electrochemical properties of supercapacitors, considerable efforts have been devoted to developing new electrode materials with higher specific capacitance and cyclical stability. Recently, some emerging nanocomposite materials (i.e., wood [5], nanocellulose [6], MOFs [7,8], and Mxene [9], etc.) are increasingly used as electrode materials to apply in energy-related fields.

Among them, biomass-derived carbon-based electrodes have attracted extensive attention and application due to their low cost, rich sources, environmental protection, and superior capacitive energy storage performance [10–13]. Wood composed of well-connected hollow fibrous structures exhibits abundant oxygen-containing functional groups [14] that

can act as active sites for chemical modifications facilitating the in-situ functionalization with polymers or inorganic materials [15–17]. Wood-derived carbon inherits the layered honeycomb structure and interconnected large porosity of natural wood and can provide multi-scale directional channels for ion transport [18–21]. In addition, unlike toner, wood-derived carbon can be directly used as self-supporting electrodes without collectors, additives, and adhesives [22,23]. These show that wood-derived carbon is an ideal 3D framework substrate to support electroactive components as freestanding electrodes for high-performance energy-storage devices.

Transition metal oxides (TMOs) mainly contribute higher capacitance to the whole capacitor due to the change of multiple valence states of transition metals. However, metal oxides have the disadvantages of low electronic conductivity, limited stability, and rapid loss of their capacity during cycling [24,25]. In order to solve these problems, combining TMOs and wood-derived carbon is a surprising way to greatly improve their electrochemical performance. For example, Wang et al. prepared a ZnO-loaded/PC composite [26]. Deng et al. synthesized a Co_3O_4 /3DGN/NF hybrid [27]. Li et al. prepared Co_3O_4 nanospheres embedded in nitrogen-doped carbon framework [28]. They improved the electrochemical properties of composites by surface attachment, anchoring, or fully embedding TMOs into the carbon skeleton.

Zeolite imidazole framework (ZIF) is a well-known MOF structure with high surface area, easy synthesis at room temperature, and inherent nitrogen doping on carbon [24–27]. In recent years, the combination of ZIFs and wood is considered to be a challenge full of opportunities [29,30]. In this paper, we report a simple and general strategy for preparing hybrid ZIFs derived Zn doped Co_3O_4 semi-embedded in wood-derived carbon skeleton ($\text{Zn-Co}_3\text{O}_4$ @CW-230) composite electrode. Compared with ZIF-67, which is easy to collapse under high-temperature calcination, the Co^{2+} -excess bimetallic hybrid Co/Zn ZIFs (HZs) [31] is more stable in structure. HZs-derived carbon acts as the electrical highway and mechanical backbone to prevent Co_3O_4 from gathering so that the $\text{Zn-Co}_3\text{O}_4$ @CW-230 electrode has excellent electrochemical activity. Compared with surface composites and fully-embedded composites, $\text{Zn-Co}_3\text{O}_4$ /C-230 particles greatly increase the specific surface area of carbonized wood, and semi-embedded structure can improve the stability of electrode materials and shorten the electron/ion transport path, accelerating the reaction kinetics.

2. Results and Discussion

Natural wood (poplar wood) can be considered a biopolymer nanocomposite that exhibits well-aligned wood cell walls. The wood cell walls are generally composed of oriented cellulose microfibrils and the matrix of lignin and hemicellulose [32]. As shown in Figure 1, first, the pre-cut poplar slices were pretreated with an alkali solution. This process simultaneously fulfills two main functions: (i) it ensures the ion exchange of the proton in the wood inherent carboxyl groups by sodium cations, providing the nucleation sites for the subsequent growth of the HZs structure, and (ii) it provides a rough fibrillar structure that boosts the anchoring of the HZs to the wood [33]. Then, a layer of HZs was semi-embedded on the inner and outer surfaces of the pretreated wood by the vacuum impregnation method, which is helpful in embedding its derivatives in the carbonized wood in situ. The second step: the $\text{Zn-Co}_3\text{O}_4$ @CW-230 was obtained by consecutive carbonization and oxidation at different calcination temperatures. Semi-embedded $\text{Zn-Co}_3\text{O}_4$ /C-230 particles can be used as energy storage nodes, while wood-derived carbon can be used as a collector and support to promote full contact between electrolyte and electrode materials and rapid transfer of electrons/ions.

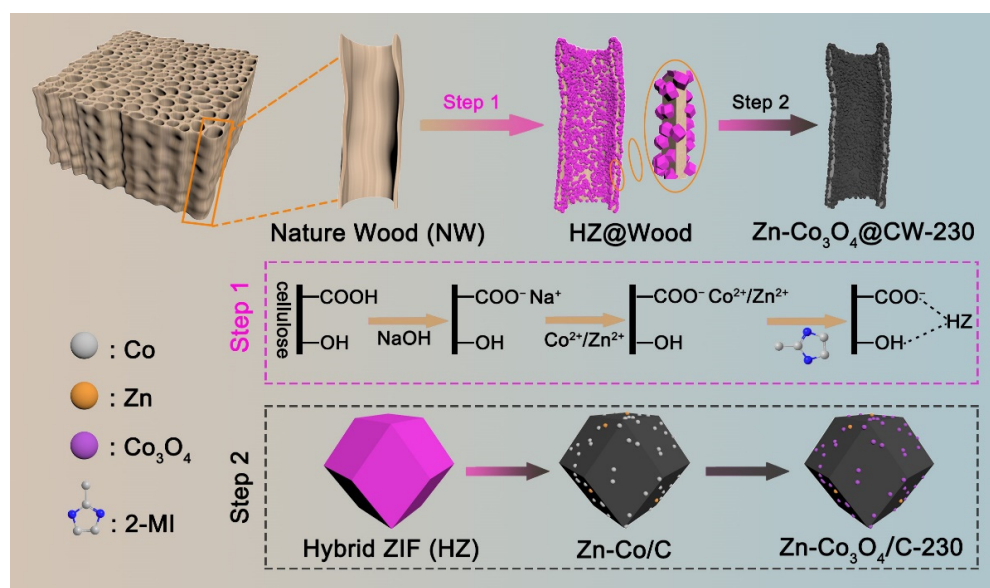


Figure 1. Schematic representation of the fabrication procedure for Zn-Co₃O₄@CW-230.

The scanning electron microscopy (SEM) images (Figures S1 and S2a–c) display a typical natural wood structure for carbonized wood with vertical channels and hierarchical porosity. On the internal section of HZ@Wood, it can be observed that a layer of dodecahedral HZs is evenly semi-embedded on the inner and outer surfaces of the wood (Figure 2a–c). Compared with ZIFs of a single metal base, during the calcination of Co²⁺-based ZIF-67, its polyhedral structure will collapse due to the formation of Co nanoparticles (NPs) (Figure S2d–f) [34,35]. In Figure S2g–i, it can be observed that the wood-derived carbon skeleton of Zn@CW-230 is smooth and complete, and there is no embedded active substance, which proves that ZIF-8 cannot penetrate the wood-derived carbon skeleton. Excitingly, Zn-Co₃O₄/C-230 particles can maintain the polyhedral morphology of ZIFs well, although their size shrinks slightly due to the decomposition of organic ligands (Figure 2a–i). Among them, by further enlarging the wood-derived carbon skeleton, it can be clearly seen that the dodecahedral particles are embedded in the wood-derived carbon skeleton, and the SEM energy mapping images show that the Co and Zn elements go deep into the wood-derived carbon skeleton (Figure 2j). The content of active substances in the material was analyzed by TG data. In Figure S3, the weight loss curve of Zn-Co₃O₄@CW-230 shows that the content of active substances in the sample is 11.46 wt%. According to the energy-dispersive X-ray spectrogram, the relative atomic ratio (%) of the Zn-Co₃O₄@CW-230 sample is obtained (Table S1). [36] The results show that the oxidation of Co NPs is dominant in the oxidation process, Zn exists in the form of doping, and its atomic percentage is very low (0.21%).

In the XRD pattern (Figure 3a), the main diffraction peaks of Zn-Co@CW come from carbon and Co, which are basically consistent with WC/Co-800 [37]. The Zn-Co@CW and Zn-Co₃O₄@CW-230 samples deliver two broad diffraction peaks at ~26° and ~45°, assigned to the (004) and (102) planes of carbon (PDF no. 26-1080). It can be seen from the spectrogram that after carbonization, the crystallinity of wood embedded in HZs is higher than that of pure wood. This is because a large amount of HZs-derived carbon with higher crystallinity will be derived on the electrode surface. In this process, the Co diffraction peak (PDF no. 15-0806) disappears, and the Co₃O₄ (PDF no. 43-1003) diffraction peak appears, indicating that Co NPs are indeed oxidized to Co₃O₄. Interestingly, Co NPs originated from HZs, which indicates that HZs grow successfully on wood. Figure 3b shows the Raman spectrum of CW, CW-230, Zn-Co@CW, and Zn-Co₃O₄@CW-230 samples. The D band around 1340 cm⁻¹ corresponds to defective/disordered carbon, while the G band around 1590 cm⁻¹ and the 2D band around 2690 cm⁻¹ correspond to typical peaks of sp² hybridized graphitic carbons observed in Raman spectra of Zn-Co₃O₄@CW-

230 [35]. The ratio of D and G peak strengths (I_D/I_G) is used to analyze the defects and crystallinity of carbon material. The I_D/I_G ratio of Zn-Co@CW and CW is the same at 0.93. After oxidation in air, the ratio of Zn-Co₃O₄@CW-230 and CW-230 decreases because more crystalline carbon is exposed due to the decomposition of amorphous carbon on the electrode surface. It is worth noting that the I_D/I_G ratio of Zn-Co₃O₄@CW-230 is reduced to 0.85 may be because the electrode surface with a semi-embedded structure is more conducive to the decomposition of amorphous carbon. This may mean greater conductivity and less resistance.

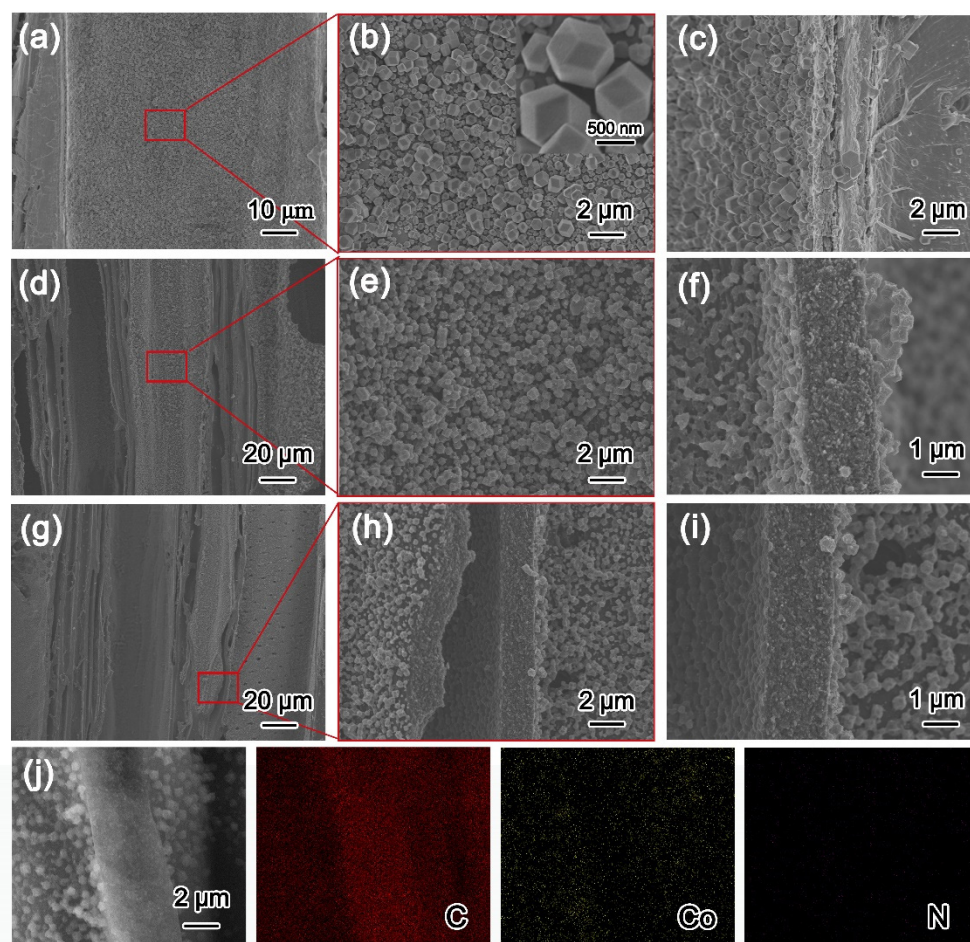


Figure 2. SEM images of HZ@Wood (a–c), Zn-Co@CW (d–f), and Zn-Co₃O₄@CW-230 (g–i); C, Co, Zn mapping of Zn-Co₃O₄@CW-230 (j).

The chemical composition and valence of all samples are analyzed by the XPS test. No signal peak of Zn can be detected in the survey spectrum because the Zn-relative components are very low (Figure 3c). However, the peaks at 1021.88 and 1045.05 eV can be detected in Zn@CW-230 belonging to Zn 2p_{3/2} and Zn 2p_{1/2} (Figure S4a). Compared with Zn@CW, after oxidation, both peaks have a slight shift. As shown in Figure 3d, the high-resolution spectrum of C 1s has four peaks at 284.3, 284.9, 287.5, and 289.0 eV, corresponding to the characteristic signals of C–C, C–O/C–N, C=O, and O–C=O bonds, respectively [38,39]. It can be seen from Figure S4b that the oxidation process in the air greatly increases the oxygen-containing functional groups on carbonized wood, which may improve the hydrophilicity of electrode materials. The high-resolution Co spectrum is fitted by Co⁰, Co²⁺, Co³⁺, and satellite peaks, as shown in Figures 3e and S4c. The peak at 780.6 eV in the Co 2p_{3/2} region belongs to oxidized Co species (Co²⁺). The main peak of Zn-Co@CW at 778.15 eV belongs to Co 2p_{3/2}, which comes from the zero-valence state of Co. The main peak of Zn-Co₃O₄@CW-230 at 779.6 eV belongs to Co 2p_{3/2}, which comes

from Co^{3+} [36,40,41]. This indicates that the simple substance Co is completely oxidized to Co_3O_4 with a better energy storage effect.

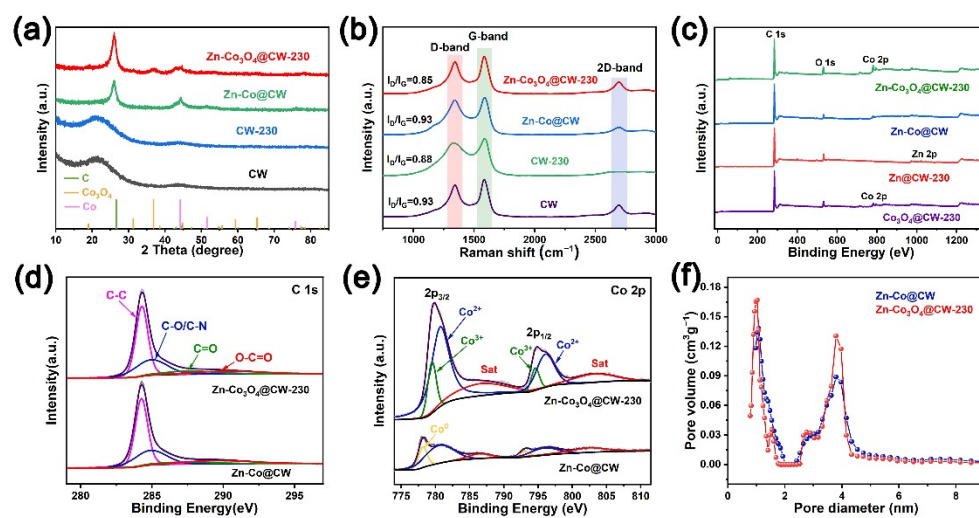


Figure 3. (a) XRD spectra of CW, CW-230, Zn-Co@CW, and Zn- Co_3O_4 @CW-230; and Raman spectra (b). XPS spectra of (c) full scan survey for Co_3O_4 @CW-230, Zn@CW-230, Zn-Co@CW, and Zn- Co_3O_4 @CW-230. High-resolution XPS spectra of Zn-Co@CW and Zn- Co_3O_4 @CW-230 for (d) C 1s and (e) Co 2p; and (f) corresponding pore size distribution.

The N_2 adsorption and desorption tests reveal the coexistence of many micropores/mesopores in the Zn- Co_3O_4 @CW-230 (Figure 3f). These pores are critical for ion adsorption and diffusion in electrochemical processes [42]. As shown in Figure S4d, the adsorption isotherm of Zn- Co_3O_4 @CW-230 is type IV, and the hysteresis loop of adsorption isotherm is type H4, which has a clear micropore filling phenomenon at low pressure [35]. The generation of type H4 hysteresis loop shows that mesopores increase, which is consistent with the data of the aperture distribution diagram. The specific surface area of Zn-Co@CW and Zn- Co_3O_4 @CW-230 are 270.6 and $300 \text{ m}^2 \text{ g}^{-1}$, and the pore size distribution is mainly located at 1.0, 2.8, and 3.8 nm, respectively. These prove that Zn- Co_3O_4 @CW-230 has more micropores and mesopores, a larger specific surface area, and may obtain greater energy storage capacity.

All sample electrodes were subjected to cyclic voltammetry (CV), and galvanostatic charge-discharge (GCD) tests on the three-electrode system (Figure 4, Figures S5 and S6). Cyclic voltammetry tests are performed on the electrodes at scan rates of 5, 10, 15, 20, and 30 mV s^{-1} , and the CV curve of all samples demonstrates a slightly distorted quasi-rectangular shape, indicating the formation of electrical double layers with representative electrostatic ion sorption and desorption [43]. The current response value and loop area of the Zn- Co_3O_4 @CW-230 in the voltage window of $-1\sim 0 \text{ V}$ are the largest, indicating that the Zn- Co_3O_4 @CW-230 has the highest capacity. GCD testing of all sample electrodes at current densities of $5\sim 30 \text{ mA cm}^{-2}$, the ideal isosceles triangle charge-discharge curve reveals the good electrochemical performance and fast mass transfer rate of wood-derived carbon materials. The area-specific capacitances of Zn- Co_3O_4 @CW-230 are 7.83, 7.47, 7.05, 6.82, and 6.46 F cm^{-2} at current densities of 5, 10, 15, 20, and 30 mA cm^{-2} , respectively (Figure 4b). The area-specific capacitances of CW-230, Zn@CW-230, and Co_3O_4 @CW-230 are 2.32, 6.03, and 4.46 F cm^{-2} at 10 mA cm^{-2} , respectively (Figure S6). This is due to the high conductivity of wood-derived carbon substrate and easy electrolyte penetration, and better utilization of Co_3O_4 electroactive surface in the redox reaction [44,45], which is consistent with the results inferred from the previous characterization. In Figure 4d, the electrochemical performances were further explored by EIS, and the Nyquist plots were fitted with an equivalent circuit diagram (Figure S8). R_s is the internal solution resistance, including the inherent resistance of the material, the ionic resistance of the electrolyte,

and the contact resistance between the material and the electrolyte. R_{ct} represents the charge transfer resistance [46], and W is the Warburg impedance represented by the line slope in the low-frequency region, which affects the diffusion rate of electrolyte ions in the electrode material. The Nyquist plots of Co@CW, Co₃O₄@CW-230, Zn-Co@CW, and Zn-Co₃O₄@CW-230 with R_{Ω} resistance values of 3.00, 2.61, 3.35, and 2.98 Ω , respectively, show extraordinary conductivity.

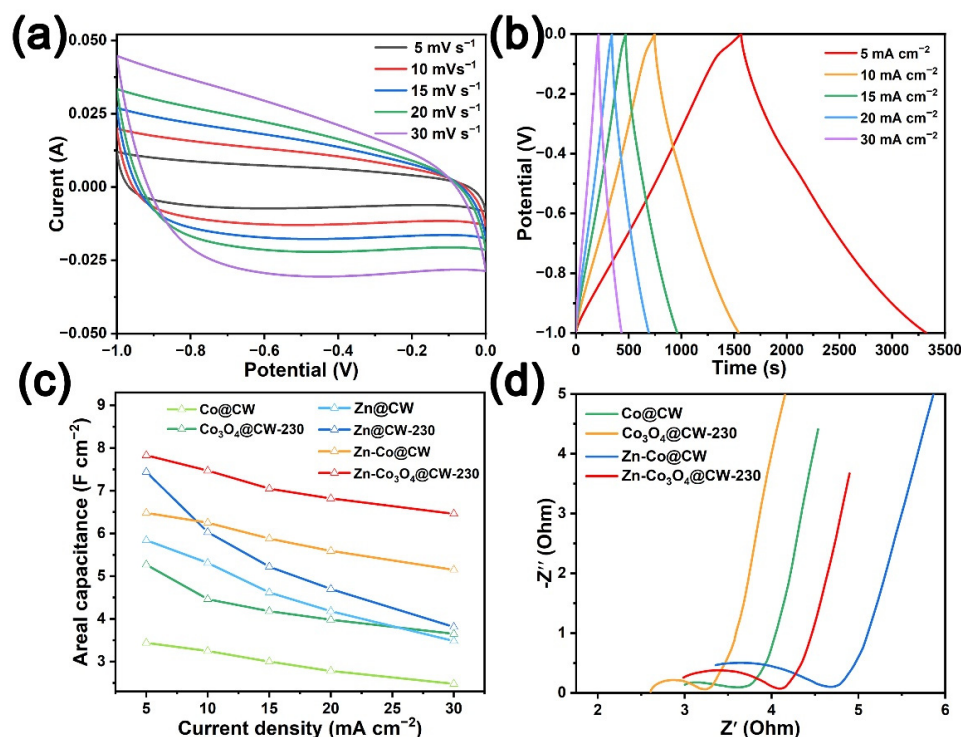


Figure 4. Cyclic voltammograms (CVs) at different scan rates and galvanostatic charge-discharge (GCD) curves at different current densities of (a,b) Zn-Co₃O₄@CW-230. (c) Specific capacitances of Zn/Co/Zn-Co@CW and Zn/Co₃O₄/Zn-Co₃O₄@CW-230 at different current densities. (d) the EIS plots of the Co/Zn-Co@CW and Co₃O₄/Zn-Co₃O₄@CW-230.

To investigate the application potential of CW-230, Co₃O₄@CW-230, and Zn-Co₃O₄@CW-230 electrodes in liquid-state SCs, we assembled CW-230//CW-230, Co₃O₄@CW-230//Co₃O₄@CW-230, and Zn-Co₃O₄@CW-230//Zn-Co₃O₄@CW-230 symmetrical SCs. Figures 5a,b and S9 are the GCD test and CV test of the above SCs. It can be seen from the test results that the CV curves of CW-230//CW-230 and Co₃O₄@CW-230//Co₃O₄@CW-230 are not regular rectangles, indicating that their electric double layer energy storage behavior has changed. Moreover, the areal-specific capacities of the CW-230//CW-230 and Co₃O₄@CW-230//Co₃O₄@CW-230 SCs are only 0.618 F cm⁻² at 2.0 mA cm⁻² and 2.35 F cm⁻² at 5.0 mA cm⁻². However, the CV curves of Zn-Co₃O₄@CW-230//Zn-Co₃O₄@CW-230 SC at different scan speeds (Figure 5a) still maintain an ideal rectangle, which is due to the surface of Zn-Co₃O₄@CW-230 electrode has higher conductivity and mechanical stability, benefiting from the semi-embedded design and more stable structure of Zn-Co₃O₄/CW-230 particles. The area-specific capacitance of Zn-Co₃O₄@CW-230//Zn-Co₃O₄@CW-230 SC reaches 2.61, 2.39, 2.24, 2.11, and 1.89 F cm⁻² at 5, 10, 15, 20 and 30 mA cm⁻², respectively (Figure 5c), maintaining excellent rate performance. This SC also exhibits the superior energy densities of 0.36 mWh cm⁻² (6.0 mWh cm⁻³) at the power densities of 2.5 mW cm⁻², which surpasses CW-230//CW-230 and Co₃O₄@CW-230//Co₃O₄@CW-230 (Figure 6). It is worth noting that the 0.6 mm thick monolithic electrode is also an important performance indicator when assembling the SC. In order to further evaluate the energy storage performance of materials, the data of energy/power density of different SC devices are compared in Table S2 [39,47–53]. The excellent energy density of Zn-Co₃O₄@CW-

230//Zn-Co₃O₄@CW-230 SC is significantly higher than other SC equipment. Furthermore (Figure 5d), the capacitance of Zn-Co₃O₄@CW-230//Zn-Co₃O₄@CW-230 SC remains at 97.3% after cycling for 10,000 cycles at 50 mA cm⁻². The capacities of CW-230//CW-230, Co₃O₄@CW-230//Co₃O₄@CW-230, and Zn@CW-230//Zn@CW-230 SCs fluctuated greatly during long cycles at high current densities, and their capacity retention ratios fluctuated in the range of 90~105%. The results show that the symmetric SC assembled with Zn-Co₃O₄@CW-230 electrode exhibits excellent electrical conductivity, ion transport rate, and cycling stability.

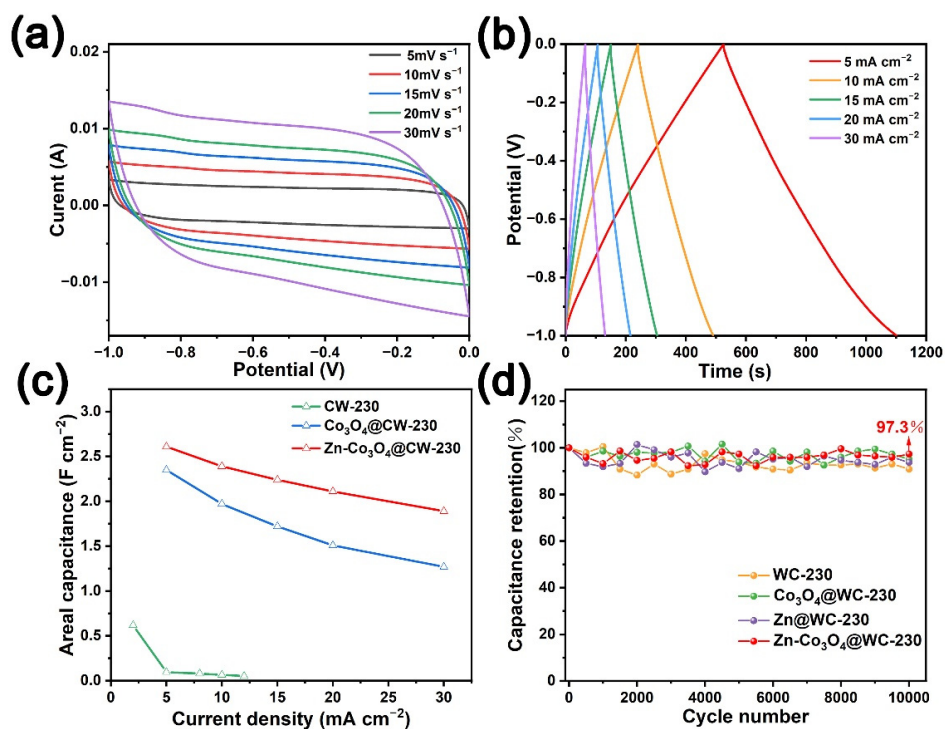


Figure 5. Capacitive performance of the SC of Zn-Co₃O₄@CW-230: (a) cyclic voltammograms at various scan rates in a two-electrode system, and (b) GCD profiles at different current densities. (c) Rate performances based on the GCD curves at different current densities, (d) the SC device measured at 50 mA cm⁻² for 10,000 cycles.

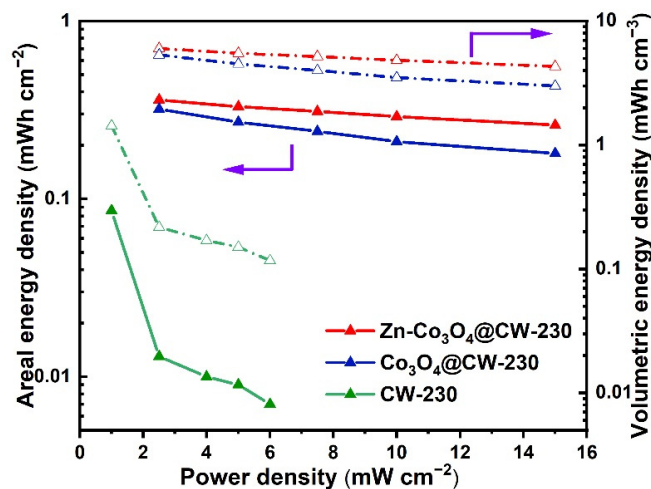


Figure 6. Areal energy density and volumetric energy density at different power densities of the SC of CW-230, Co₃O₄@CW-230, and Zn-Co₃O₄@CW-230.

3. Materials and Methods

3.1. Materials

Cobalt nitrate hexahydrate ($\text{Co}(\text{NO}_3)_2 \cdot 6\text{H}_2\text{O}$, 99%), Zinc nitrate hexahydrate ($\text{Zn}(\text{NO}_3)_2 \cdot 6\text{H}_2\text{O}$, 99%), 2-methylimidazole (2-MI), sodium hydroxide (NaOH), and Potassium hydroxide (KOH) were obtained from Aladdin and used directly. The Poplar wood block used in this study was received from a wood processing factory in the south of China. All reagents are of analytical-grade and used without further purification. Deionized (DI) water was used as the solvent.

3.2. Wood Pretreatment

Poplar monoliths were cut into cuboids with the dimensions $40 \times 40 \times 4 \text{ mm}^3$ (radial \times tangential \times longitudinal, $R \times T \times L$). The slices were then immersed in a 15 wt% NaOH aqueous solution for 1 h. Afterward, the slices were thoroughly rinsed with deionized water until the pH reached 9. Finally, the pretreated wood was dehydrated by freeze-drying.

3.3. Preparation of HZ@Wood

The pretreated wood slices were immersed in a mixed solution for 2 h, which was prepared by dissolving $\text{Co}(\text{NO}_3)_2 \cdot 6\text{H}_2\text{O}$ (1.16 g) and $\text{Zn}(\text{NO}_3)_2 \cdot 6\text{H}_2\text{O}$ (0.59 g) in methanol/deionized water (30/5 mL). A 2-MeIm solution prepared by dissolving 9.85 g of 2-MI in methanol/deionized water (30/5 mL) was dropwise added and stirred at ambient temperature for 24 h. The HZ/Wood was washed with methanol and freeze-dried in a vacuum. ZIF-8@Wood and ZIF-67@Wood were developed in the same way.

3.4. Preparation of Zn-Co@CW and Zn-Co₃O₄@CW-230

HZ@Wood was put into a tube furnace under temperature programming and constant Ar flow. The sample was heated slowly from room temperature to 700 °C with a heating rate of 5 °C/min, maintained for 5 h under an Ar atmosphere. After that, the furnace was naturally cooled to room temperature in an Ar atmosphere to obtain black powders, denoted as Zn-Co@CW. Then, Zn-Co₃O₄@CW-230 was obtained by further calcining Zn-Co@CW in an air atmosphere at 230 °C for 1 h at the same heating rate. In addition, we prepared Co@CW, Zn@CW, CW, Co₃O₄@CW-230, Zn@CW-230, and CW-230 from ZIF-67@Wood and ZIF-8@Wood and pure wood by the same preparation method.

3.5. Characterization and Electrochemical Testing

The morphology and structure were characterized by scanning electron microscopy (SEM, Hitachi SU8010). The phase composition of as-obtained materials was analyzed by an X-ray diffraction instrument (XRD, Bruker D8). The surface chemical information was detected by X-ray Photoelectron Spectroscopy (XPS, ThermoFisher ESCALAB 250Xi). The specific surface area and hierarchical porous structure were measured by automatic surface area and porosity analysis (Brunauer–Emmett–Teller (BET), MicroActive ASAP2020). Raman spectroscopy (Raman, LabRAM HR Evolution) was used to test the chemical states of the carbon atoms. Thermogravimetric (TG) analyses were carried out on a thermogravimeter (TGA5500) from room temperature to 800 °C in the air with a heating rate of 10 °C min⁻¹.

The electrochemical performances of a single electrode were tested with a three-electrode setup on an electrochemical workstation (Vertex.One/Vertex.C, IVIUM, Eindhoven, The Netherlands) by using an Hg/HgO as the reference electrode, a platinum plate as the counter electrode, and a 6M KOH aqueous solution as the electrolyte. As shown in Figure S10, 6M KOH aqueous solution is also used as an electrolyte to assemble a two-electrode device to test the liquid-state symmetric SCs.

4. Conclusions

In conclusion, we found that HZs could be used as precursors to obtain a monolithic electrode with semi-embedded active substances on the surface. The inner and outer surface structure of wood-derived carbon was modified by derived Zn-Co₃O₄/C-230 particles, which greatly improved the specific surface area of carbonized wood and the electrochemical and mechanical stability of electrodes. In addition, the step of oxidation in the air is also crucial. It not only improves the crystallinity of carbon-reducing electrode resistance but also will obtain TMOs with better energy storage effect. Based on the above advantages, the area-specific capacitance of Zn-Co₃O₄@CW-230 can reach 7.83 F cm⁻² at current densities of 5.0 mA cm⁻² (0.6 mm thick). The areal-specific capacitance of assembled Zn-Co₃O₄@CW-230//Zn-Co₃O₄@CW-230 SC is as high as 2.61 F cm⁻² at 5.0 mA cm⁻², and it shows great energy densities of 0.36 mWh cm⁻² (6.0 mWh cm⁻³), due to its high-capacity contribution of Co₃O₄, unique semi-embedded structure, and conductivity. The strategy of semi-embedding the TMOs derived from ZIFs into wood-derived carbon is expected to promote the development of other ZIFs and wood composites and provide a new research idea for the large-scale production of high-performance charcoal self-supporting composite electrodes and the practical application of high energy density SCs.

Supplementary Materials: The following supporting information can be downloaded at: <https://www.mdpi.com/article/10.3390/molecules27238572/s1>, Figure S1: SEM of the poplar wood slice: perpendicular to the growth direction at different magnification times; Table S1: Analysis results of energy dispersive X-ray spectrogram; Figure S2: SEM images of nature wood; Table S2: Comparison of electrochemical performance of SC of Zn-Co₃O₄@CW-230 and some representative carbon-/metal oxide-based electrodes at device level; Figure S3: TGA curves of Zn@CW-230, Co₃O₄@CW-230, Zn-Co₃O₄@CW-230 composites in air; Figure S4: XPS spectra of Zn@CW and Zn@CW-230 for Zn 2p; Figure S5: Cyclic voltammograms (CVs) at different scan rates and galvanostatic charge–discharge curves at different current densities; Figure S6: Cyclic voltammograms (CVs) at different scan rates and galvanostatic charge–discharge curves at different current densities; Figure S7: Specific capacitances of CW, CW-230 at different current densities; Figure S8: Equivalent circuit diagram fitted by Nyquist diagram; Figure S9: CVs at different scan rates and GCD curves at different current densities; Figure S10: Photos of a two-electrode system of the Zn-Co₃O₄@CW-230 liquid-state SC.

Author Contributions: Conceptualization, W.X. and J.O.; methodology, W.X.; software, X.W.; validation, X.W., J.O. and X.W.; formal analysis, Z.H.; investigation, L.Z.; resources, M.L.; data curation, Y.L. (Yuxin Lu) and W.Y.; writing—original draft preparation, W.X.; writing—review and editing, G.L. and C.Z.; visualization, X.W. and W.Y.; supervision, Y.L. (Yongfeng Luo); project administration, Y.L. (Yongfeng Luo) and B.X.; funding acquisition, G.L. and C.Z. All authors have read and agreed to the published version of the manuscript.

Funding: This research was funded by the Natural Science Foundation of China, grant numbers 31890771, 21908251, and 42074016, Hunan Provincial Natural Science Foundation of China, grant numbers 2021JJ31148 and 2020JJ5962.

Institutional Review Board Statement: Not applicable.

Informed Consent Statement: Not applicable.

Data Availability Statement: The data used to support these findings have been included in this article. Additional information is available from the corresponding authors upon request.

Acknowledgments: This work was supported by the Natural Science Foundation of China (No. 31890771, 21908251, and 42074016), Hunan Provincial Natural Science Foundation of China (No. 2021JJ31148 and 2020JJ5962); the authors would like to thank Yu Lu of Shiyanjia Lab (www.shiyanjia.com) for SEM analysis.

Conflicts of Interest: The authors declare no conflict of interest.

References

1. Simon, P.; Gogotsi, Y.; Dunn, B. Where Do Batteries End and Supercapacitors Begin? *Science* **2014**, *343*, 1210–1211. [[CrossRef](#)] [[PubMed](#)]
2. Ouyang, J.; Wang, X.M.; Wang, L.C.; Xiong, W.N.; Li, M.Y.; Hua, Z.H.; Zhao, L.L.; Zhou, C.; Liu, X.B.; Chen, H.; et al. Construction of a porous carbon skeleton in wood tracheids to enhance charge storage for high-performance supercapacitors. *Carbon* **2022**, *196*, 532–539. [[CrossRef](#)]
3. Xiao, J.; Han, J.W.; Zhang, C.; Ling, G.W.; Kang, F.Y.; Yang, Q.H. Dimensionality, Function and Performance of Carbon Materials in Energy Storage Devices. *Adv. Energy Mater.* **2022**, *12*, 2100775. [[CrossRef](#)]
4. Lin, T.Q.; Chen, I.W.; Liu, F.X.; Yang, C.Y.; Bi, H.; Xu, F.F.; Huang, F.Q. Nitrogen-doped mesoporous carbon of extraordinary capacitance for electrochemical energy storage. *Science* **2015**, *350*, 1508–1513. [[CrossRef](#)] [[PubMed](#)]
5. Jiao, M.L.; Liu, T.; Chen, C.J.; Yue, M.; Pastel, G.; Yao, Y.G.; Xie, H.; Gan, W.T.; Gong, A.; Li, X.F.; et al. Holey three-dimensional wood-based electrode for vanadium flow batteries. *Energy Storage Mater.* **2020**, *27*, 327–332. [[CrossRef](#)]
6. Guo, R.Q.; Zhang, L.X.; Lu, Y.; Zhang, X.L.; Yang, D.J. Research progress of nanocellulose for electrochemical energy storage: A review. *J. Energy Chem.* **2020**, *51*, 342–361. [[CrossRef](#)]
7. Lin, J.; Reddy, R.C.K.; Zeng, C.H.; Lin, X.M.; Zeb, A.; Su, C.Y. Metal-organic frameworks and their derivatives as electrode materials for potassium ion batteries: A review. *Coord. Chem. Rev.* **2021**, *446*, 214118. [[CrossRef](#)]
8. Giannakoudakis, D.A.; Bandoz, T.J. Building MOF Nanocomposites with Oxidized Graphitic Carbon Nitride Nanospheres: The Effect of Framework Geometry on the Structural Heterogeneity. *Molecules* **2019**, *24*, 4529. [[CrossRef](#)]
9. Li, X.L.; Huang, Z.D.; Shuck, C.E.; Liang, G.J.; Gogotsi, Y.; Zhi, C.Y. MXene chemistry, electrochemistry and energy storage applications. *Nat. Rev. Chem.* **2022**, *6*, 389–404. [[CrossRef](#)]
10. Yang, C.H.; Xiong, J.W.; Ou, X.; Wu, C.F.; Xiong, X.H.; Wang, J.H.; Huang, K.; Liu, M.L. A renewable natural cotton derived and nitrogen/sulfur co-doped carbon as a high-performance sodium ion battery anode. *Mater. Today Energy* **2018**, *8*, 37–44. [[CrossRef](#)]
11. Cao, W.X.; Yang, F.Q. Supercapacitors from high fructose corn syrup-derived activated carbons. *Mater. Today Energy* **2018**, *9*, 406–415. [[CrossRef](#)]
12. Prasankumar, T.; Salpekar, D.; Bhattacharyya, S.; Manoharan, K.; Yadav, R.M.; Miller, K.A.; Vajtai, R.; Jose, S.; Roy, S.; Ajayan, P.M. Biomass derived hierarchical porous carbon for supercapacitor application and dilute stream CO₂ capture. *Carbon* **2022**, *199*, 249–257. [[CrossRef](#)]
13. Yuan, J.; Wang, Y.; Zhao, X.; Chen, H.; Chen, G.; Wang, S. Seven years of biochar amendment has a negligible effect on soil available P and a progressive effect on organic C in paddy soils. *Biochar* **2022**, *4*, 1. [[CrossRef](#)]
14. Yang, J.; Li, H.; He, S.; Du, H.; Liu, K.; Zhang, C.; Jiang, S. Facile Electrodeposition of NiCo₂O₄ Nanosheets on Porous Carbonized Wood for Wood-Derived Asymmetric Supercapacitors. *Polymers* **2022**, *14*, 2521. [[CrossRef](#)] [[PubMed](#)]
15. Li, Z.; Wang, X.; Wang, Z.; Wang, L.; Guo, Y.; Zhou, C.; Li, X.; Du, K.; Luo, Y. Nickel-cobalt layered double hydroxide nanosheets anchored to the inner wall of wood carbon tracheids by nitrogen-doped atoms for high-performance supercapacitors. *J. Colloid Interface Sci.* **2022**, *608*, 70–78. [[CrossRef](#)]
16. Wang, X.; Deng, Y.; Wang, Z.; Li, Z.; Wang, L.; Ouyang, J.; Zhou, C.; Luo, Y. Sophora-like Nickel–Cobalt Sulfide and Carbon Nanotube Composites in Carbonized Wood Slice Electrodes for All-Solid-State Supercapacitors. *ACS Appl. Energy Mater.* **2022**, *5*, 7400–7407. [[CrossRef](#)]
17. Wu, W.; Wang, X.; Deng, Y.; Zhou, C.; Wang, Z.; Zhang, M.; Li, X.; Wu, Y.; Luo, Y.; Chen, D. In situ synthesis of polyaniline/carbon nanotube composites in a carbonized wood scaffold for high performance supercapacitors. *Nanoscale* **2020**, *12*, 17738–17745. [[CrossRef](#)]
18. Ma, Y.; Yao, D.X.; Liang, H.Q.; Yin, J.W.; Xia, Y.F.; Zuo, K.H.; Zeng, Y.P. Ultra-thick wood biochar monoliths with hierarchically porous structure from cotton rose for electrochemical capacitor electrodes. *Electrochim. Acta* **2020**, *352*, 136452. [[CrossRef](#)]
19. Liu, K.; Mo, R.W.; Dong, W.J.; Zhao, W.; Huang, F.Q. Nature-derived, structure and function integrated ultra-thick carbon electrode for high-performance supercapacitors. *J. Mater. Chem. A* **2020**, *8*, 20072–20081. [[CrossRef](#)]
20. Wang, Y.M.; Lin, X.J.; Liu, T.; Chen, H.; Chen, S.; Jiang, Z.J.; Liu, J.; Huang, J.L.; Liu, M.L. Wood-Derived Hierarchically Porous Electrodes for High-Performance All-Solid-State Supercapacitors. *Adv. Funct. Mater.* **2018**, *28*, 1806207. [[CrossRef](#)]
21. Karthaus, J.; Biziks, V.; Mai, C.; Militz, H. Lignin and Lignin-Derived Compounds for Wood Applications—A Review. *Molecules* **2021**, *26*, 2533. [[CrossRef](#)]
22. Cao, M.M.; Liu, Y.Y.; Sun, K.; Li, H.; Lin, X.Q.; Zhang, P.X.; Zhou, L.M.; Wang, A.; Mehdi, S.; Wu, X.L.; et al. Coupling Fe₃C Nanoparticles and N-Doping on Wood-Derived Carbon to Construct Reversible Cathode for Zn-Air Batteries. *Small* **2022**, *18*, 2202014. [[CrossRef](#)] [[PubMed](#)]
23. Huang, J.L.; Zhao, B.T.; Liu, T.; Mou, J.R.; Jiang, Z.J.; Liu, J.; Li, H.X.; Liu, M.L. Wood-Derived Materials for Advanced Electrochemical Energy Storage Devices. *Adv. Funct. Mater.* **2019**, *29*, 1902255. [[CrossRef](#)]
24. Liu, R.; Zhou, A.; Zhang, X.R.; Mu, J.B.; Che, H.W.; Wang, Y.M.; Wang, T.T.; Zhang, Z.X.; Kou, Z.K. Fundamentals, advances and challenges of transition metal compounds-based supercapacitors. *Chem. Eng. J.* **2021**, *412*, 128611. [[CrossRef](#)]
25. Kong, L.L.; Wang, L.; Sun, D.Y.; Meng, S.; Xu, D.D.; He, Z.X.; Dong, X.Y.; Li, Y.F.; Jin, Y.C. Aggregation-Morphology-Dependent Electrochemical Performance of Co₃O₄ Anode Materials for Lithium-Ion Batteries. *Molecules* **2019**, *24*, 3149. [[CrossRef](#)] [[PubMed](#)]
26. Shen, X.Y.; Mu, D.B.; Chen, S.; Wu, B.R.; Wu, F. Enhanced Electrochemical Performance of ZnO-Loaded/Porous Carbon Composite as Anode Materials for Lithium Ion Batteries. *ACS Appl. Mater. Interfaces* **2013**, *5*, 3118–3125. [[CrossRef](#)] [[PubMed](#)]

27. Deng, X.Y.; Li, J.J.; Zhu, S.; He, F.; He, C.N.; Liu, E.Z.; Shi, C.S.; Li, Q.F.; Zhao, N.Q. Metal-organic frameworks-derived honeycomb-like Co_3O_4 /three-dimensional graphene networks/Ni foam hybrid as a binder-free electrode for supercapacitors. *J. Alloys Compd.* **2017**, *693*, 16–24. [[CrossRef](#)]
28. Li, H.H.; Zhou, L.; Zhang, L.L.; Fan, C.Y.; Fan, H.H.; Wu, X.L.; Sun, H.Z.; Zhang, J.P. Co_3O_4 Nanospheres Embedded in a Nitrogen-Doped Carbon Framework: An Electrode with Fast Surface-Controlled Redox Kinetics for Lithium Storage. *ACS Energy Lett.* **2017**, *2*, 52–59. [[CrossRef](#)]
29. Wei, Y.; Liu, R.; Liu, H.; Sun, Y.; Liu, G.; Wang, Z.; Luo, Y.; Tang, X.; Zhang, X.; Hu, J. Controllable One-Dimensional Growth of Metal–Organic Frameworks Based on Uncarved Halloysite Nanotubes as High-Efficiency Solar-Fenton Catalysts. *J. Phys. Chem. C* **2021**, *125*, 25565–25579. [[CrossRef](#)]
30. Ma, X.; Xiong, Y.; Liu, Y.; Han, J.; Duan, G.; Chen, Y.; He, S.; Mei, C.; Jiang, S.; Zhang, K. When MOFs meet wood: From opportunities toward applications. *Chem* **2022**, *8*, 2342–2361. [[CrossRef](#)]
31. Kim, J.; Young, C.; Lee, J.; Heo, Y.U.; Park, M.S.; Hossain, M.S.A.; Yamauchi, Y.; Kim, J.H. Nanoarchitecture of MOF-derived nanoporous functional composites for hybrid supercapacitors. *J. Mater. Chem. A* **2017**, *5*, 15065–15072. [[CrossRef](#)]
32. Chen, C.; Berglund, L.; Burgert, I.; Hu, L. Wood Nanomaterials and Nanotechnologies. *Adv. Mater.* **2021**, *33*, 2006207. [[CrossRef](#)] [[PubMed](#)]
33. Tu, K.K.; Puertolas, B.; Adobes-Vidal, M.; Wang, Y.R.; Sun, J.G.; Traber, J.; Burgert, I.; Perez-Ramirez, J.; Keplinger, T. Green Synthesis of Hierarchical Metal–Organic Framework/Wood Functional Composites with Superior Mechanical Properties. *Adv. Sci.* **2020**, *7*, 1902897. [[CrossRef](#)] [[PubMed](#)]
34. Jiang, M.; He, H.; Yi, W.J.; Huang, W.; Pan, X.; Wang, M.Y.; Chao, Z.S. ZIF-67 derived Ag- Co_3O_4 @N-doped carbon/carbon nanotubes composite and its application in Mg-air fuel cell. *Electrochem. Commun.* **2017**, *77*, 5–9. [[CrossRef](#)]
35. Ma, X.F.; Zhao, S.Y.; Tian, Z.W.; Duan, G.G.; Pan, H.Y.; Yue, Y.Y.; Li, S.S.; Jian, S.J.; Yang, W.S.; Liu, K.M.; et al. MOFs meet wood: Reusable magnetic hydrophilic composites toward efficient water treatment with super-high dye adsorption capacity at high dye concentration. *Chem. Eng. J.* **2022**, 136851. [[CrossRef](#)]
36. Guo, S.Q.; Liu, J.B.; Zhang, Q.Q.; Jin, Y.H.; Wang, H. Metal organic framework derived Co_3O_4 /Co@N-C composite as high-performance anode material for lithium-ion batteries. *J. Alloys Compd.* **2021**, 157538. [[CrossRef](#)]
37. Ma, X.; Guo, H.; Zhang, C.; Chen, D.; Tian, Z.; Wang, Y.; Chen, Y.; Wang, S.; Han, J.; Lou, Z.; et al. ZIF-67/wood derived self-supported carbon composites for electromagnetic interference shielding and sound and heat insulation. *Inorg. Chem. Front.* **2022**, *9*, 6305–6316. [[CrossRef](#)]
38. Wang, Z.H.; Wang, X.M.; Wang, L.C.; Wei, Y.; Zhao, Z.; Du, K.; Chen, D.Y.; Li, X.J.; Zhou, C.; Liu, G.G.; et al. ZIF-67-derived Co@N-PC anchored on tracheid skeleton from sawdust with micro/nano composite structures for boosted methylene blue degradation. *Sep. Purif. Technol.* **2022**, *278*, 119489. [[CrossRef](#)]
39. Zhang, W.J.; Li, M.; Zhong, L.; Huang, J.L.; Liu, M.L. A family of MOFs@Wood-Derived hierarchical porous composites as freestanding thick electrodes of solid supercapacitors with enhanced areal capacitances and energy densities. *Mater. Today Energy* **2022**, *24*, 100951. [[CrossRef](#)]
40. Qin, T.F.; Dang, S.; Hao, J.X.; Wang, Z.L.; Li, H.Q.; Wen, Y.X.; Lu, S.Q.; He, D.Y.; Cao, G.Z.; Peng, S.L. Carbon fabric supported 3D cobalt oxides/hydroxide nanosheet network as cathode for flexible all-solid-state asymmetric supercapacitor. *Dalton Trans.* **2018**, *47*, 11503–11511. [[CrossRef](#)]
41. Nuamah, R.A.; Noormohammed, S.; Sarkar, D.K. Supercapacitor performance evaluation of nanostructured Ag-decorated Co- Co_3O_4 composite thin film electrode material. *Int. J. Energ Res.* **2022**, *46*, 13099–13110. [[CrossRef](#)]
42. Ali, G.A.M.; Habeeb, O.A.; Algarni, H.; Chong, K.F. CaO impregnated highly porous honeycomb activated carbon from agriculture waste: Symmetrical supercapacitor study. *J. Mater. Sci.* **2018**, *54*, 683–692. [[CrossRef](#)]
43. Deka, B.K.; Hazarika, A.; Kim, J.; Kim, N.; Jeong, H.E.; Park, Y.B.; Park, H.W. Bimetallic copper cobalt selenide nanowire-anchored woven carbon fiber-based structural supercapacitors. *Chem. Eng. J.* **2019**, *355*, 551–559. [[CrossRef](#)]
44. Ali, G.A.M.; Fouad, O.A.; Makhoulf, S.A.; Yusoff, M.M.; Chong, K.F. Co_3O_4 /SiO₂ nanocomposites for supercapacitor application. *J. Solid State Electr.* **2014**, *18*, 2505–2512. [[CrossRef](#)]
45. Wang, X.; Wu, W.; Wang, Z.; Li, Z.; Wang, X.; Zhou, C.; Luo, Y. Cobalt Hydroxide Nanosheets Grown on Carbon Nanotubes Anchored in Wood Carbon Scaffolding for High-Performance Hybrid Supercapacitors. *Energy Fuels* **2021**, *35*, 18815–18823. [[CrossRef](#)]
46. Zheng, K.; Li, G.; Xu, C. Advanced battery-supercapacitor hybrid device based on Co/Ni-ZIFs-derived NiCo_2S_4 ultrathin nanosheets electrode with high performance. *Appl. Surf. Sci.* **2019**, *490*, 137–144. [[CrossRef](#)]
47. Tian, R.R.; Duan, C.Y.; Feng, Y.; Cao, M.J.; Yao, J.F. Metal Organic Framework-Based CoNi Composites on Carbonized Wood as Advanced Freestanding Electrodes for Supercapacitors. *Energy Fuels* **2021**, *35*, 4604–4608. [[CrossRef](#)]
48. Rafiq, M.I.; Farid, T.; Zhou, J.; Ali, A.; Tang, J.; Tang, W.H. Carbonized wood-supported hollow NiCo_2S_4 eccentric spheres for high-performance hybrid supercapacitors. *J. Alloys Compd.* **2019**, *811*, 151858. [[CrossRef](#)]
49. Wang, Z.L.; Zhu, Z.L.; Qiu, J.H.; Yang, S.H. High performance flexible solid-state asymmetric supercapacitors from MnO_2 /ZnO core shell nanorods//specially reduced graphene oxide. *J. Mater. Chem. C* **2014**, *2*, 1331–1336.
50. Zheng, Z.; Retana, M.; Hu, X.B.; Luna, R.; Ikuhara, Y.H.; Zhou, W.L. Three-Dimensional Cobalt Phosphide Nanowire Arrays as Negative Electrode Material for Flexible Solid-State Asymmetric Supercapacitors. *ACS Appl. Mater. Interfaces* **2017**, *9*, 16987–16995. [[CrossRef](#)]

51. Yang, P.H.; Ding, Y.; Lin, Z.Y.; Chen, Z.W.; Li, Y.Z.; Qiang, P.F.; Ebrahimi, M.; Mai, W.J.; Wong, C.P.; Wang, Z.L. Low-Cost High-Performance Solid-State Asymmetric Supercapacitors Based on MnO₂ Nanowires and Fe₂O₃ Nanotubes. *Nano Lett.* **2014**, *14*, 731–736. [[CrossRef](#)] [[PubMed](#)]
52. Wang, W.C.; Yuan, Y.L.; Yang, J.; Meng, L.; Tang, H.C.; Zeng, Y.J.; Ye, Z.Z.; Lu, J.G. Hierarchical core-shell Co₃O₄/graphene hybrid fibers: Potential electrodes for supercapacitors. *J. Mater. Sci.* **2018**, *53*, 6116–6123. [[CrossRef](#)]
53. Yu, N.; Zhu, M.Q.; Chen, D. Flexible all-solid-state asymmetric supercapacitors with three-dimensional CoSe₂/carbon cloth electrodes. *J. Mater. Chem. A* **2015**, *3*, 7910–7918. [[CrossRef](#)]